RESEARCH PAPER

Modelling of Hot Deformation and Dynamic Recrystallization Behavior of Boron-Bearing Low-Carbon Steel Using Hot compression Flow Curves

S. M. Mirghasemi, E. Mohammad Sharifi*, Gh. Borhani, M. S. Beigi

* e-m-sharifi@mut-es.ac.ir

Malek Ashtar University of Technology, Department of Material Science and Advanced Electromagnetic Materials

Abstract: *This study investigated the hot deformation and dynamic recrystallization behavior of low-carbon steel containing 21 ppm boron. After homogenizing the samples at 1250°C for 1 hour, hot compression tests were conducted at temperatures ranging from 850°C to 1150°C and strain rates from 0.01 to 10 s⁻¹, resulting in strain-stress flow curves. Following corrections, calculations and modelling were performed based on Arrhenius equations. Among them, the hyperbolic sine relationship provided the most accurate estimate and was selected as the valid model for the applied strain range. According to this model, the deformation activation energy (Q), was determined to be 293.37 KJ/mol. Additionally, critical and peak stress and strain values were obtained for each temperature and strain rate, and power relationships were established to describe their variation concerning the Zener-Hollomon parameter (Z). Recrystallization fractions were derived by comparing the hypothetical recovery curves with the material flow curves, and the results were successfully modelled using the Kolmogorov-Johnson-Mehl-Avrami (KJMA) equation. The Avrami exponent was measured at approximately 2, indicating that nucleation predominantly occurred at grain boundaries. Microstructural analysis revealed that at higher Z values, recrystallization occurred along with a fraction of elongated grains, while lower Z values resulted in a greater fraction of equiaxed dynamic recrystallization (DRX) grains. The average grain sizes after compression tests at 950°C, 1050°C, and 1150°C were measured as 21.9 μm, 30.4 μm, and 33.6 μm respectively at a strain rate of 0.1 s⁻¹, and 17.7 μm, 28.7 μm, and 31.3 μm at 1 s⁻¹. The overall microstructure displayed a more uniform grain size distribution with increasing deformation temperature.*

Keywords: DRX modelling, Arrhenius relations, Hot compression, Low carbon steel.

1. INTRODUCTION

Boron-containing low-carbon steels have properties such as high strength, high ductility, continuous yielding, high workability, and a low ratio of yield strength to ultimate tensile strength compared to conventional low-carbon steels [1, 2]. Segregation of boron atoms at the austenite grain boundary and reduction of energy state at those regions reduces ferrite nucleation in grain boundaries during cooling. As a result, the hardenability of steel increases [3-5], and in addition, it also improves the hot workability of steel [6, 7]. The optimum amount of boron to achieve the desired hot deformation behavior and ideal mechanical properties including strength, has been reported between 10 and 30 ppm [8-10]. Other conditions, including providing suitable cooling rates and alloying elements also have a significant effect [11, 12]. The addition of Ti and Nb to boron-bearing low-carbon steels can improve the possibility of Boron segregation in austenite grain boundaries and increase hardenability by preventing its combination with nitrogen [13-15]. Thus, it can lead to achieving a microstructure containing hard phases like martensite, bainite and pearlite in these steels, which increases the hardness and strength of steel [16]. Therefore, adding boron can improve the mechanical properties of low-carbon steels and can be a lower-cost alternative to alloying elements such as chromium, molybdenum and manganese.

Since the deformation of metals at high temperatures is influenced by the activation of high temperature microstructural deformation mechanisms and the combination of strain hardening and softening, both of which are affected by many factors such as strain, strain rate and deformation temperature, the change and the evolution of these mechanisms and deformation conditions lead to microstructural evolution, which results in changes in the mechanical and deformation behavior of materials [17, 18]. Thus, understanding the flow behavior of metals and alloys at high temperature deformation conditions is very important in terms of its effect on flow patterns and the kinetics of metallurgical transformations related to hot deformation, such as recovery and dynamic recrystallization. Therefore, fundamental numerical models are

1

used to describe the flow behavior of plastically deformable metallic materials and alloys, which can express the result of the simultaneous effect of the effective phenomenon at hot deformation in the form of relationships mathematical equations and numerical constants. These fundamental models are mainly divided into three categories: phenomenological models, physical-based models and models based on artificial neural networks. Meanwhile, the basic phenomenological models are more useful for simulating the deformation behavior of metals and alloys at high temperatures and different strain rates. Among the various phenomenological models, the Arrhenius model is one of the most well-known and widely used models for describing the fundamental behavior of materials, which is used for deformation conditions dependent on temperature, stress, strain, and strain rate [19]. Recently, significant progress has been made in correlating the hot deformation activation energy and stress exponent (n) with atomistic mechanisms across various engineering materials [20, 21].

Dynamic recrystallization (DRX), which is one of the most important active mechanisms during high temperature deformation, plays a significant role in changing the flow behavior of metallic materials and their microstructural evolutions. In general, in materials with low stacking fault energy (such as copper, nickel, and austenite in steels) that have a low dynamic recovery rate (DRV), a high density of dislocations generated during deformation remains in the microstructure up to high temperatures, which It provides the activation energy (Q) required for DRX at higher temperatures. With continuous nucleation and growth of grains during hot deformation, DRX is one of the most important factors of softening, flow behavior and microstructural evolutions in metallic materials [22, 23]. Therefore, investigating its effect during hot deformation is very important. To investigate the dynamic recrystallization kinetics, various models have been presented, which are mostly derived from the Kolmogorv-Johnson-Mehl-Avrami (KJMA) relationship [24-27].

Although a lot of research has been done in this field regarding the investigation of the hot deformation behavior of low-carbon steels with numerical modelling and the investigation of recrystallization kinetics [28-31], less research has been done on the hot deformation behavior of low carbon steels in the presence of Boron; Or if it is done, comprehensive and complete modelling has not been done using thermomechanical relationships and fundamental equations for these steels, and the effect of all influencing factors, including DRX, has not been investigated. Therefore, according to the explanations provided about the complexity of the deformation behavior of metals at high temperatures and also, the simultaneous effect of alloying elements including boron on the properties and deformation behavior of low carbon steels, this research aims to provide a comprehensive and complete modelling based on existing fundamental models of boron containing low carbon steel.

2. EXPERIMENTAL PROCEDURES

2.1. Sample Preparation and Hot Compression Condition

In this study, boron-bearing low-carbon steel with the chemical composition according to Table 1 was prepared from the continuous casting line of the Mobarakeh Steel complex in the form of sheet metal with dimensions of 20×30×2 cm. The chemical composition was obtained using Inductively Coupled Plasma (ICP) and Spark Emission Spectroscopy (SES) analysis after three repetitions, and as a result, the amount of boron was measured with an accuracy of 1 ppm. To prepare the samples for the hot compression test, the steel sheet was subjected to homogenization heat treatment at 1250°C for 60 minutes and after that, the sample cooled in the air to room temperature. After that, hot compression test samples were prepared according to ASTM-E9 standards in the form of cylinders with a diameter of 5 mm and a height of 10 mm by use of a CNC wire cut machine.

Table 1. Chemical composition of boron-bearing low-carbon steel (wt%)

Element	C	Mn	Si	P	S	Cr	Mo	Ni	V
wt%	0.053	0.476	0.007	0.007	0.0027	0.0086	0.001	0.0225	0.0029
Element	Cu	Al	As	Sn	Nb	Ti	N	B	Fe
wt%	0.007	0.383	0.0013	0.0037	0.0002	0.0007	0.0023	0.0021	balance

2

The hot compression test was performed at temperatures of 850, 950, 1050 and 1150°C and strain rates 10, 1, 0.1 and 0.01 s^{-1}. First, each sample was heated to 1200°C and kept at that temperature for 5 minutes, and then it was cooled to the compression test temperature with a cooling rate of 5°C/s. Then the hot pressure test was performed with different strain rates by 50% reduction in the height of the samples. The schematic diagram of this thermomechanical process is shown in Figure 1. After that, the samples were cut in half using a wire-cut machine, and the cut surface was prepared by sanding and polishing, followed by etching, for microstructural analysis by scanning electron microscope (SEM), Energy-dispersive X-ray spectroscopy (EDS) and optical microscope (OM). Microstructural images were analyzed using MIP image analysis software and the average and distribution of grain sizes were obtained. Since it is difficult to measure the exact amount of light elements such as nitrogen and boron using EDS analysis, it is not possible to accurately measure the chemical composition of precipitates and phases in the microstructure. For this reason, using JMatPro thermodynamic analysis software, the chemical composition of the alloy was investigated and the formation of possible phases and compounds in the equilibrium state was investigated.
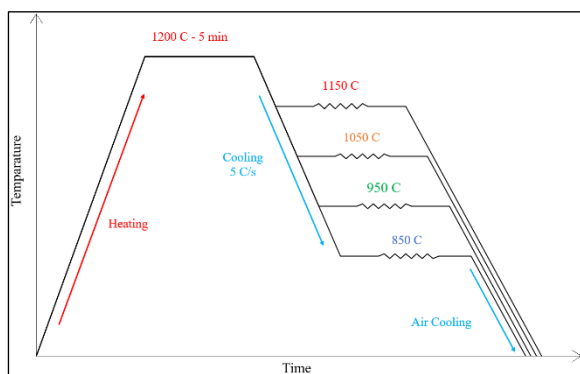

Fig. 1. Schematic diagram of the hot compression process

2.2. Stress-Strain Corrections and Flow Curves

After performing hot compression tests on the samples and obtaining the true stress-strain curves, the results were subjected to two corrections to reduce the test errors. The first case is the effect of friction, which increases the stress compared to the actual value. Equation 1 [32] was used to correct the stress values and eliminate the effect of friction:

$$\sigma_a = \sigma_0 \left(1 + 2\frac{m}{3\sqrt{3}}\frac{R}{H}\right) \tag{1}$$

In this relation, σ_a is the applied stress, σ_0 is the flow stress, m is the friction coefficient, R is the radius and H is the actual height of the sample. Also, another form of this relation can be used as relation 2 [33]:

$$\sigma_a = \sigma_0 \left(1 + 2\frac{m}{3\sqrt{3}}\frac{R_0}{H_0}\right)\exp\left(\frac{3\varepsilon}{2}\right) \tag{2}$$

Here, R_0 and H_0 are the initial values of the radius and height of the sample, and their actual value is applied by applying the strain ε in the relation. The method proposed by Ebrahimi and Najafizadeh was also used to calculate the friction coefficient m [34]. In their method, the dimensions of the sample after the compression test are used to calculate the friction coefficient. It should be noted that by calculating the values of the friction coefficient for different samples, it was observed that the value of m is more dependent on the test temperature and its values were calculated almost close to each other at a constant temperature. The average values of the friction coefficient m for hot compression test samples at temperatures of 850, 950, 1050 and 1150°C were calculated as 0.36, 0.48, 0.60 and 0.71 respectively.

The next correction that was applied to the stress-strain data is related to the error produced due to the heat caused by the deformation and the increase in the temperature of the sample during the compression test. This increase in temperature causes the force and stress data to be measured less than the actual values. According to research, about 5% of the energy input to the material is spent on metallurgical processes, and about 95% of it is converted into heat. In perfect adiabatic conditions, the entire heat generated in the sample is used to raise its temperature. Otherwise, a fraction of this heat is used to raise the temperature of the sample [35], which is considered efficiency according to the following equation:

$$\eta = \frac{\Delta T_{actual}}{\Delta T_{adiabatic}} \tag{3}$$

As a result, the following equation can be used to calculate the actual temperature change of the sample:

$$\Delta T_{actual} = \frac{0.95\,\eta}{\rho C_p}\int \sigma_a d\varepsilon \tag{4}$$

In this relation, ρ is the density of the substance and C_p is its specific heat capacity at constant

pressure. Considering that both the strain and the strain rate have an effect on the shape and dimensions of the sample and the actual heat flux in the sample, therefore, the method proposed by Goetz and Semiatin can be used to calculate the value of η [36]. This method takes into account the effect of dimensional change during deformation on the heat flux of the sample and its temperature increase. This increase in temperature has reduced the strength of the material by $\Delta\sigma$, which should be added to the amount of stress. Therefore, the amount of $\Delta\sigma$ can be calculated according to the following equation:

$$\Delta\sigma = \Delta T_{actual}\left(\frac{d\sigma}{dT}\right)_{\varepsilon,\dot{\varepsilon}} \tag{5}$$

By performing the mentioned corrections on the stress-strain data, the corrected data have been used in the following. For example, Figure 2 shows the stress-strain curve of the hot compression test sample at a temperature of 1150°C and a strain rate of 1 s^{-1} in three different states. As can be seen in this figure, after applying friction correction on the initial raw data, the stress values decreased to lower values, and also after correcting the effect of deformation temperature, the stress values increased to higher values. It is obvious that, as expected, these changes were obtained similarly for all samples after correction.

Fig. 2. stress-strain curve of the hot compression test at a temperature of 1150°C and a strain rate of 1 s^{-1} before and after modifications

2.3. Mathematical Calculations and Curve Fitting

According to the research, the recrystallization starts from the critical strain, which occurs at a strain lower than the peak strain. The method that is suggested to find the exact value of the critical strain using flow curves, is based on the calculation of the stress-strain curve slope. According to this method, if an equation for the relationship between true stress and true strain at constant strain rate and temperature can be expressed as $\sigma = f(\varepsilon)$, the work hardening exponent is expressed as $\theta = df(\varepsilon)/d\varepsilon$. According to this relationship, the critical strain value is obtained by finding the root of the $d^2\theta/d\sigma^2$ curve in terms of strain [37]. By performing calculations for simplification, the above relation is rewritten as follows:

$$\left(\frac{d^2\theta}{d\sigma^2}\right)_{\varepsilon,T} = \left(\frac{f'''f' - (f'')^2}{(f')^3}\right)_{\varepsilon,T} \tag{6}$$

f', f'' and f''' are the first, second and third derivatives of the relation $\sigma = f(\varepsilon)$, respectively. For this purpose and to find the acceptable equation that fits the stress-strain data well, the Origin 2019 software package was used. At each temperature and strain rate, a 9th degree polynomial equation was fitted on the stress-strain data so that the coefficient of determination R^2 of each equation was very close to 1 (all above 0.99). This makes it much easier and more possible to perform mathematical calculations, including derivation on the data, compared to the primary data that has noises and errors. Also, to model the crystallization kinetics, it is necessary to perform a non-linear fitting of the recrystallization fraction data found in each sample in terms of time, and to do this, the mentioned software was used. Similarly, the R^2 coefficient close to 1 for all samples confirmed the accuracy of the calculations.

3. RESULTS AND DISCUSSION

3.1. Strain-Stress Flow Curves

Figure 3 shows the stress-strain curve of the hot compression test of boron-bearing low-carbon steel samples used in this research at different temperatures and strain rates. As it is clear in this figure, the behavior of the material, which shows the natural behavior of metals in high temperature deformation, at low temperatures and high strain rates, the curves show more dynamic recovery behavior and peak stress is not observed (at temperature 850°C and strain rates 10 and 1 s^{-1}) and with the reduction of the strain rate and the increase of the temperature, the peak stress is gradually observed in the curves. This is due to the lack of ideal thermomechanical conditions

4

such as temperature and strain rate suitable for the activation of recrystallization mechanisms. At high strain rates and low temperatures, the dislocation formation rate is higher than its annihilation rate, because the necessary conditions for the diffusion phenomenon, which is one of the main reasons for the activity of recrystallization mechanisms, are not provided. Therefore, work hardening is always observed in samples and recovery is the main mechanism in general [38]. As the temperature increases and the strain rate decreases, the continued deformation leads to the generation and increase of the dislocation density in the sample, and the energy stored as a result provides the activation energy for recrystallization. For this reason, it can be seen in the stress-strain curves of Figure 3 that the peak stress is not observed at the temperature of 850°C, except at the strain rate of 0.01 s^{-1} which occurred as a partial peak in the curve. By increasing the temperature to 950°C, peaks are observed in all strain rates except the strain rate of 10 s^{-1}, And with a further increase in temperature up to 1050 and 1150°C, peak stress is observed in all cases, which indicates the full activity of recrystallization mechanisms. It can also be seen that at any temperature, with the increase of the strain rate, the occurrence of peak stress is shifted to larger strains, which can be explained by the previous explanations.

Another thing that can be seen in the stress-strain curves is that at high temperatures and low strain rates, the curves fluctuate probably because of dynamic strain aging. In metal alloys with interstitial atoms of alloying elements, the presence of these atoms can lock the dislocations by creating interaction and being placed in the core of dislocations, and it is possible to continue sliding of dislocations by applying more stress, and after that, due to the high temperature and the possibility of the diffusion of these interstitial atoms, as well as the low strain rate and the low rate of slip of the dislocations, the interstitial atoms diffuse into the core of the dislocations again, and this repeated cycle becomes the cause of stress fluctuations [39, 40]. In low-carbon steels with a similar chemical composition containing interstitial elements such as B, N, and C, the same behavior as described has been observed and reported in other studies [41, 42].
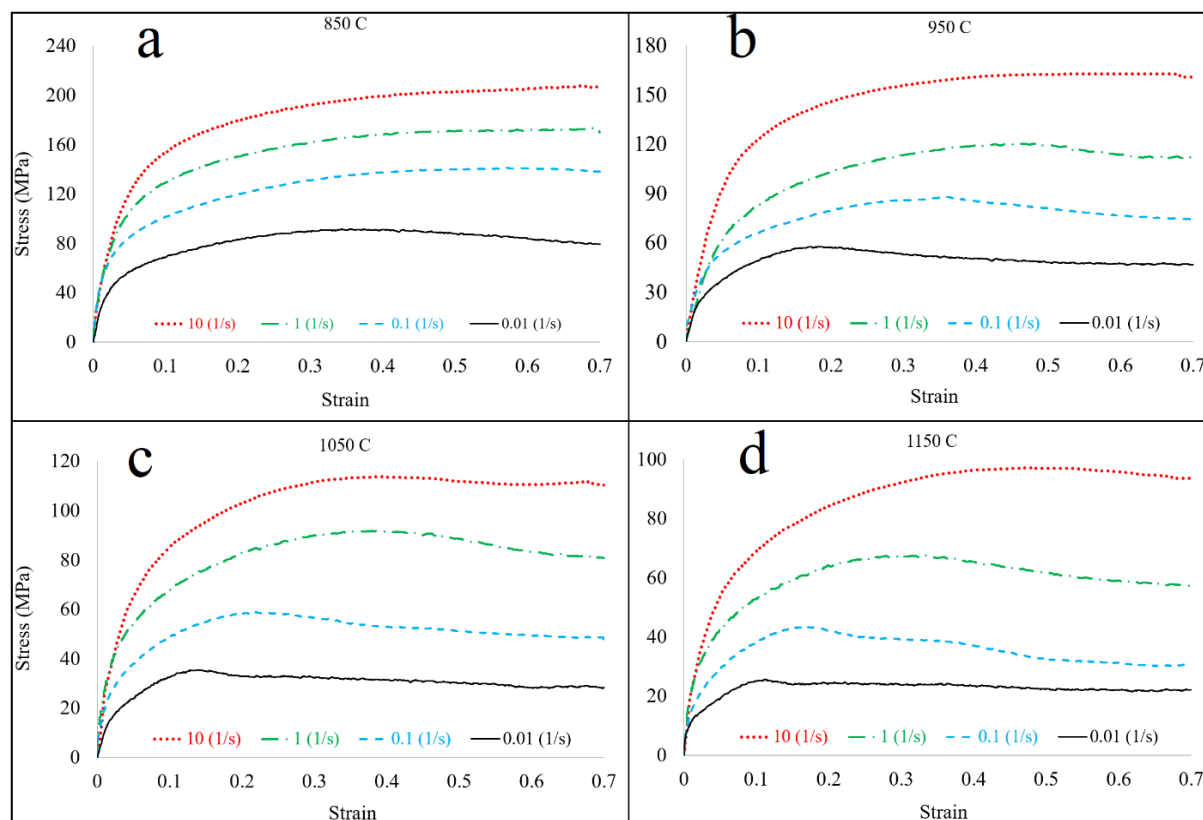

Fig. 3. Stress-strain curve of compression test at temperatures a) 850°C, b) 950°C, c) 1050°C and d-1150°C at different strain rates

E. Mohammad Sharifi et al.

3.2. Arrhenius Relations, Constitutive Equations and Constants

To investigate the relationship between stress-strain curves with temperature and strain rate as the most important factors of thermomechanical processes, the Zener-Hollomon equation is suggested, which is expressed as equation 7 [19]:

$$Z = \dot{\varepsilon} \exp(\frac{Q}{RT}) \tag{7}$$

In this equation, Q is the activation energy, T is the deformation temperature and R is the universal gas constant. According to this relationship, decreasing the strain rate and increasing the deformation temperature means decreasing the Z parameter and vice versa. On the other hand, to investigate the relationship between the Zener-Hollomon parameter and the material's flow stress, various functions have been suggested for different deformation conditions. The power relation to model the deformation behavior of materials in low strains which corresponds to low stresses, the exponential relationship I used to model the deformation behavior of materials at high strains and which corresponds to high stresses, and the hyperbolic sine relationship is used to model the deformation behavior of materials in all stress and strain conditions, which is shown in relations 8, 9 and 10, respectively [43]:

$$Z = A \, \sigma^{n'} \qquad \text{(At low } \dot{\varepsilon}\&\sigma) \tag{8}$$
$$Z = B \exp(\beta\sigma) \qquad \text{(At high } \dot{\varepsilon}\&\sigma) \tag{9}$$
$$Z = C \, [\sinh(\alpha\sigma)]^n \qquad \text{(At any } \dot{\varepsilon}\&\sigma) \tag{10}$$

In these equations, A, B, C, n', β, n and α are the material constants. By combining each of equations 8, 9 and 10 with equation 7, and applying the natural logarithm to the formed relations, the general equations that express the effect of stress, strain rate and temperature simultaneously are formed in three forms, which can be seen in equations 11, 12 and 13. Due to the difference in these equations, the difference of their activation energy is considered as an index for Q. To find the constants in these equations, by simplifying, relations 14 to 19 are obtained to find n', β, n, Q_1, Q_2 and Q_3 respectively:

$$\ln\dot{\varepsilon} = \ln A + n'\ln\sigma - \frac{Q_1}{RT} \qquad \text{(At low } \dot{\varepsilon}\&\sigma) \tag{11}$$
$$\ln\dot{\varepsilon} = \ln B + \beta\sigma - \frac{Q_2}{RT} \qquad \text{(At high } \dot{\varepsilon}\&\sigma) \tag{12}$$
$$\ln\dot{\varepsilon} = \ln C + n\ln[\sinh(\alpha\sigma)] - \frac{Q_3}{RT} \quad \text{(At any } \dot{\varepsilon}\&\sigma) \tag{13}$$
$$n' = (\frac{\partial\ln\dot{\varepsilon}}{\partial\ln\sigma})_{\varepsilon,T} \tag{14}$$
$$\beta = (\frac{\partial\ln\dot{\varepsilon}}{\partial\ln\sigma})_{\varepsilon,T} \tag{15}$$
$$n = (\frac{\partial\ln\dot{\varepsilon}}{\partial\ln[\sinh(\alpha\sigma)]})_{\varepsilon,T} \tag{16}$$
$$Q_1 = (\frac{\partial\sigma}{\partial(\frac{1}{T})})_{\varepsilon,\dot{\varepsilon}} \tag{17}$$
$$Q_2 = (\frac{\partial\ln\sigma}{\partial(\frac{1}{T})})_{\varepsilon,\dot{\varepsilon}} \tag{18}$$
$$Q_3 = (\frac{\partial\ln[\sinh(\alpha\sigma)]}{\partial(\frac{1}{T})})_{\varepsilon,\dot{\varepsilon}} \tag{19}$$

To find the value of the above constants, according to whether high or low strains are used in each relation, the stresses corresponding to the strains of 0.2 and 0.6 from the stress-strain curves of Figure 3 were used for calculations. Figures 4-a, 4-b and 4-c show the values obtained according to relations 14, 15 and 16, respectively, and the linear regression between these points at each temperature. By averaging the slope of these lines, the values of n', β and n are obtained respectively. By having the value of β and n', a relatively accurate approximation of the value of α can be calculated in the form of α= β/n' [43], which is used to calculate the value of n in equation 16. Similarly, to calculate the values of Q_1, Q_2 and Q_3, the values obtained according to relations 17 to 19 and the linear regression between these data at different strain rates are shown in Figures 4-d, 4-e and 4-f. By averaging the slopes of these lines, the activation energy values are obtained according to each relationship. After that, by having the constants obtained according to relations 11 to 13, by adding the values of Q/RT to the intercepts of the lines corresponding to each relation and performing mathematical calculations, the value of the constants A, B and C is obtained. All of these obtained constants can be seen in Table 2:

To compare the obtained results and validate them, the constants of Table 1 were placed in relations 8 to 10, and the Zener-Hollomon parameter for each temperature and strain rate was obtained by inserting the corresponding activation energy of each relation. By applying the natural logarithm of the obtained data, Figure 5 is plotted, linear regression is applied to the data, and the trend of changes in each graph and R^2 for the fitted lines is shown in the figure. According to this figure, the hyperbolic sine relationship is a more accurate model for expressing the relationship between stress-strain data under different conditions of temperature, strain rate, and strain, because in both low strain (0.2) and high strain (0.6) it has estimated the data with higher R^2 than other models (0.989 and 0.988).

6

Fig. 4. Natural logarithm values related to a- Power function b- Exponential function and c- Hyperbolic sine function, and inverse values of absolute temperature in terms of natural logarithm related to d- Power function e-Exponential function and f- Hyperbolic sine function, along with a linear regression at different temperatures and strain rates

Table 2. Values of obtained constants related to Arrhenius relations

strain	Value		Constant
0.2	6.882		n'
0.6	0.071		β
0.2, 0.6	0.010		α
0.6	4.359		n
0.2	0.037		A
0.6	4.84	$\times 10^9$	B
0.6	3.67	$\times 10^{11}$	C
0.6	313.21	KJ/mol	Q_1
0.2	299.18	KJ/mol	Q_2
0.6	293.37	KJ/mol	Q_3

Fig. 5. Natural logarithm of the functions: (a, b) power, (c, d) exponential and (e, f) hyperbolic sine, in terms of natural logarithm of their Z values

Therefore, the activation energy estimated by this model, Q3= 293.37 KJ/mol, is considered the activation energy of the steel investigated in this study. After calculating the constants and using relations 7 to 13, the general constitutive equation for this steel is obtained as follows:

$$\ln Z = \ln \dot{\varepsilon} + \frac{293370}{8.314 \times T} = 31.234 + 4.359 \times \sinh(0.01\sigma) \qquad (20)$$

In recent studies on engineering materials, the relationship between influencing parameters such as deformation activation energy and stress capacity and microstructural mechanisms on the atomic scale of materials has been shown. The amount of activation energy calculated for the steel investigated in this research is different from other research on similar low-carbon boron steels. For example, Stumpf and Banks [31], in research conducted on the hot deformation behavior of two low-carbon steels with a boron content of 4 and 11 ppm, the value of activation energy Q for two samples was reported as 351 and 388 KJ/mol, respectively. The reason for the difference in the value of Q in the two samples is reported to be due to the solute drag effect of boron atoms and the delay of softening mechanisms in the sample

8

with more boron content. In this case, much research on the combined effect of boron and other alloying elements has been conducted, including the research conducted by Liu et al [6] and Cho et al. [44]. In total, these researches have shown that in similar low-carbon steel alloys with boron, the amount of boron can affect the amount of fine AlN precipitate particles, which are among the particles that by locking the grain boundaries and dislocations, have a great impact on the hot deformation behavior of these steels. This means that an increase in the amount of boron leads to an increase in the formation of coarse BN particles at a temperature higher than the temperature of AlN formation, and a lower amount of AlN is formed and scattered in the microstructure. As a result, this can lead to even more activity of softening mechanisms and recrystallization. Therefore, the conclusion is that the effect of boron on the hot working behavior of low-carbon steels is completely dependent on the chemical composition and the conditions created in the presence of other alloying elements. In this study, the formation and precipitation of AlN and BN have been investigated in part 3.5.

3.3. Characteristic Stresses and Strains of the Material

According to the explanations in the previous sections, in high temperature deformation by applying strain, recrystallization starts at a strain lower than the peak strain called critical strain (ε_c), which by plotting the values of equation 6 in terms of strain and obtaining the root of this equation, the value of critical strain is obtained.

Also, due to the presence of the first-order derivative in the denominator of this relationship, a vertical asymptote appears in the graph, which indicates the peak strain (ε_p). The mentioned curve for the hot compression sample at 1050°C and strain rate of 0.1 s^{-1} can be seen in Figure 6-a. The stress corresponding to these strains is known as critical stress (σ_c) and peak stress (σ_p). Also, by plotting the graph of θ in terms of σ, the peak and critical stress values are determined on the graph, which is shown for the hot compression sample at 1050°C and strain rate 0.1 s^{-1} in Figure 6-b. Other parameters that can be obtained from this curve are mentioned in the figure. If at the critical point, which is the inflection point of the θ-σ curve, a tangent line is plotted on the curve so that its extension intersects the horizontal axis, the point where the tangent line meets the horizontal axis is the saturated stress value (σ_s) in the hypothetical condition without recrystallization, which is used to calculate the hypothetical recovery curve equation and compare with the actual curve to calculate the recrystallization fraction [45]. More explanations about this are given in the following sections. Also, the value of the steady state stress (σ_{ss}) is obtained when the curve meets the horizontal axis again. These characteristic strain and stress values for all compression test samples were obtained according to the stress-strain curves in Figure 3 and plotted diagrams similar to Figures 6-a and 6-b, which are presented in Table 3. As it is clear in the table, some values such as peak strain, peak stress and steady state stress are not mentioned for some samples.

Fig. 6. a) d$^2\theta$/dσ^2 curve in terms of strain, b) θ-σ curve, for the hot compression test sample at 1050°C and a strain rate of 0.1 s^{-1}

[DOI: 10.22068/ijmse.3512]

Table 3. Characteristic parameters of samples at different temperatures and strain rates

Temperature (°C)	Strain rate (s⁻¹)	ε_c	σ_c (MPa)	ε_p	σ_p (MPa)	σ_{ss} (MPa)	σ_s (MPa)
850	10	0.343	195.3	-	-	-	217.2
	1	0.337	164.5	-	-	-	180.6
	0.1	0.152	111.8	0.599	140.7	-	162.8
	0.01	0.140	75.2	0.371	90.9	-	132.4
950	10	0.342	158.0	0.628	162.8	-	169.3
	1	0.328	115.1	0.451	120.0	111.9	132.4
	0.1	0.145	72.8	0.340	86.6	74.3	120.6
	0.01	0.102	49.5	0.196	57.6	47.0	81.1
1050	10	0.176	99.7	0.395	113.5	110.5	127.6
	1	0.167	78.7	0.385	91.5	80.8	103.6
	0.1	0.103	49.1	0.224	58.5	48.0	73.5
	0.01	0.066	24.9	0.139	35.1	32.5	61.6
1150	10	0.179	81.6	0.477	97.0	93.5	106.7
	1	0.145	58.6	0.303	67.3	57.2	79.7
	0.1	0.098	37.8	0.165	43.2	30.2	59.5
	0.01	0.073	22.7	0.110	25.3	21.8	36.1

The reason is that in the range of strain applied on the mentioned samples, according to the temperature and applied strain rate, peak stress or steady state stress could not occur. The absence of peak stress in the range of applied strain can be due to the non-occurrence of recrystallization at the deformation temperature, or the peak stress may occur with continued deformation at higher strains.

By comparing the data in Table 3, it can be seen that with increasing temperature and decreasing strain rate, the values of stress and critical and peak strain are decreasing. Therefore, these changes can be expressed by the value of the Zener-Holman parameter in the form of a power relation.

Using equation 13 and the deformation activation energy calculated in the previous sections, the natural logarithm of *Z* is plotted in terms of the natural logarithm of the critical and peak stress and strain data in Figure 7, and the linear regression of these data along with R^2 can be seen in this figure. According to this figure and the fitting performed on the data, the characteristic stress and strain values in terms of the Z parameter are obtained in the form of the following relations:

$$\varepsilon_c = 4.27 \times 10^{-3} \times Z^{0.135} \qquad (21)$$
$$\varepsilon_p = 3.79 \times 10^{-3} \times Z^{0.169} \qquad (22)$$
$$\sigma_c = 7.79 \times 10^{-1} \times Z^{0.172} \qquad (23)$$
$$\sigma_c = 8.68 \times 10^{-1} \times Z^{0.170} \qquad (24)$$

3.4. Kinetics of Dynamic Recrystallization

The kinetics of recrystallization is the result of the opposition between the kinetics of plastic deformation and the kinetics of restoration processes, which are in conflict with each other in the multiplication and annihilation of dislocations.
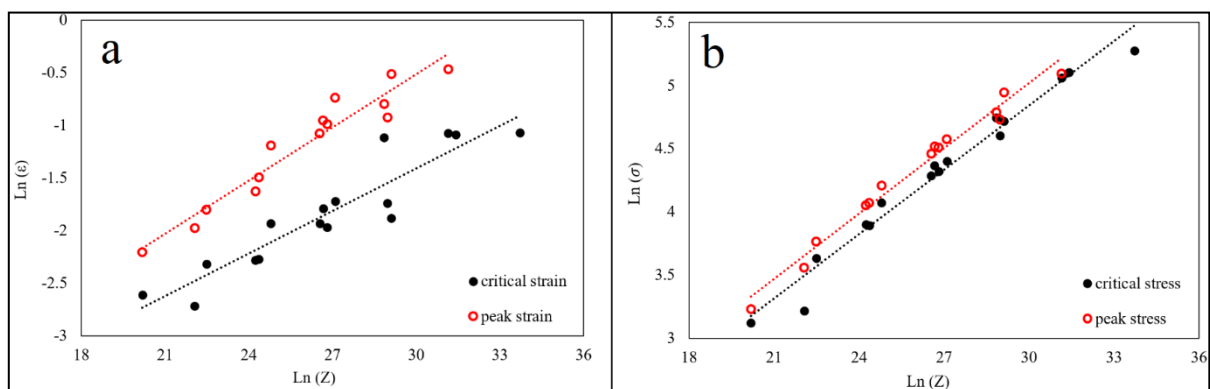
Fig. 7. a) critical and peak strain, b) critical and peak stress, according to the values of Z

Therefore, to accurately describe the kinetics of recrystallization, models based on the density of mobile dislocations in the material are presented and used, the most common form of which is equation 25 [46]:

$$\frac{d\rho}{d\varepsilon} = k_1 - k_2\rho \qquad (25)$$

In this equation, ρ is the density of dislocations in the material, k_1 is a constant to express the increase in density and the non-thermal accumulation of mobile dislocations, and k_2 is a constant to express the thermal mechanisms of restoration and recovery of dislocations, including their annihilation and rearrangement in the material during deformation at high temperature. According to the relations presented for the deformation behavior of metallic materials using the density of moving dislocations, the hypothetical flow curve can be defined that only with the increase in the density of dislocations, the flow stress increases with work-hardening and it reaches its limit value in high strains, which is called the dynamic recovery curve or work-hardening curve (σ_{WH}). To obtain the equation of this hypothetical dynamic recovery curve, the actual flow curves of the material in the hot compression test can be used; So that at the critical point, which is the initiation of the recrystallization process, the recovery curve and the flow curve of the material are separated. In the recovery curve, only work hardening occurs under the influence of increasing dislocation density until it reaches its limit value which is the saturated stress (σ_s) where the dislocation density has reached its limit value [47].

Therefore, with mathematical calculations based on the effect of dislocation density on the material's flow stress and by using the material's actual flow curves, equation 26 [47] is used to express the hypothetical work-hardening or recovery curve:

$$\sigma_{WH} = [\sigma_s^2 + (\sigma_1^2 - \sigma_s^2)\exp(-k_2\Delta\varepsilon)]^{0.5} \qquad (26)$$

In this relation, k_2 is the constant of the material, σ_s is the saturated stress or the limiting value of the recovery curve, σ_1 is the stress at a point before the critical point, and $\Delta\varepsilon$ is the difference between the strain at any point of the curve and the strain ε_1 at a point before the critical point. The slope of the $\sigma\theta$-σ^2 curve is used to calculate k_2. Figure 8-a shows this curve for the hot compression test at 1050°C and a strain rate of 0.1 s^{-1}. By plotting this curve up to the critical point, as can be seen, the slope of the curve changes from non-linear to linear.

It has been confirmed that the slope of the curve at the end of the non-linear region, which is equal to the slope of the linear region, is $-0.5k_2$. In other words, to find the slope of this area of the graph, the critical point at the end of the curve and a point in the linear part of the curve are used, which is shown in Figure 8-a. Also, the intercept of this line shows the value of $0.5k_2\sigma_s^2$, which can be used to calculate the σ_s. But as mentioned in the previous section, the plotted line in Figure 6-b is used to calculate that. By obtaining the unknown values of equation 26, the σ_{WH} curve can be plotted for each sample. As an example, in Figure 8-b, the actual flow curve of the material is shown next to the recovery curve for the hot compression test sample at 1050°C and a strain rate of 0.1 s^{-1}.

Fig. 8. a) $\sigma\theta$-σ^2 curve and b) flow curve and dynamic recovery curve, related to the hot compression test at 1050°C and strain rate 0.1 s^{-1}

In the calculations made to achieve the equation of σ_{WH}, the general equation is formed based on the fact that the curve between two points $(\varepsilon_1, \sigma_1)$ and $(\varepsilon_c, \sigma_c)$ is tangent to the flow curve and from the critical point onwards, the dynamic recovery curve is separated from the original curve. Therefore, the recovery curve is only desired after the critical point, and before the critical point, both curves are considered equal [47].

By obtaining the dynamic recovery curve σ_{WH} and comparing it with the flow curve of the material, the recrystallization fraction can be obtained according to the following equation:

$$X_{drx} = \frac{\sigma_{WH} - \sigma}{\sigma_s - \sigma_{ss}} \qquad (27)$$

According to this relation, by dividing the difference between flow curve and dynamic recovery curve in each strain, with its limit value in high strains i.e., saturated stress σ_s and steady state stress σ_{ss}, the value of recrystallization fraction is calculated. By having the values of the recrystallization fraction for the samples at different temperatures and strain rates, Equation 28, rewritten from the general form of the KJMA equation, has been used to model the recrystallization kinetics:

$$X_{drx} = 1 - \exp(-k\left[\frac{\varepsilon - \varepsilon_c}{\dot{\varepsilon}}\right]^{n_A}) \qquad (28)$$

Where k and n_A are constants. In this equation, the time factor, which is replaced by a function of strain and strain rate, is obtained by using the amount of strain and strain rate in each sample; So that at the critical point, time is zero and this point is considered the origin of time, and it changes towards positive times as the deformation continues. Because in the samples where the desired values of equation 27 are not available (such as the value of σ_{ss} for some samples according to Table 3), it is not possible to calculate the recrystallization fraction and obtain the constants of equation 28, for other samples by using this relation, the recrystallization fraction values were obtained and then modelled with the KJMA equation. Figure 9 shows the values of the recrystallization fraction and Avrami model for each sample in different deformation conditions. As shown in the figure, the presented equation models the experimental data with good accuracy. Also, by comparing the graphs of different samples, it can be seen that at a constant temperature and with a decrease in the strain rate, the initiation time of recrystallization has increased to longer times.
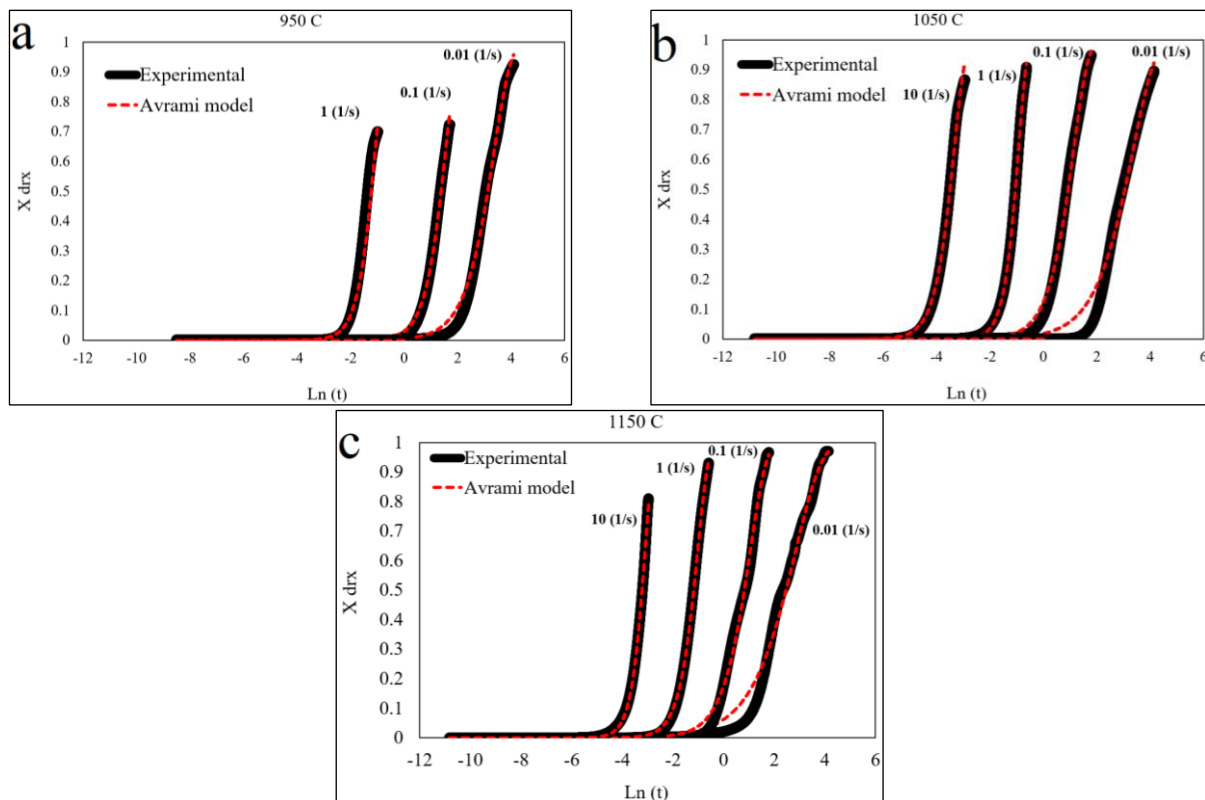

Fig. 9. X_{DRX} and Avrami model for hot compression curves at a) 950°C, b) 1050°C, c) 1150°C and different strain rates

12

At higher strain rates, the dislocation density required for recrystallization in the material is generated in a shorter time, and recrystallization initiates in a shorter time. On the other hand, because the dislocation multiplication rate is higher than its annihilation rate, a decrease in the amount of recrystallized fraction is observed in deformed samples with higher strain rates [48]. It can also be seen in this figure that with the increase in temperature, which leads to an increase in the activity of the softening mechanisms and the annihilation of dislocations, the recrystallization fraction has increased, and at lower strains and times compared to lower temperatures, the dislocation density required to reach activation energy of recrystallization is provided.

The final result of this modelling is that by using the data obtained from equation 27 and the model used in equation 28, the Avrami exponent n_A for the investigated steel was obtained as 2.03. According to the research, n_A varies between approximately 0.5 and 4, which is independent of the transformation temperature, and depends on the DRX nucleation mechanism. By increasing the n_A from 0.5 to 4, the nucleation mechanism gradually changes from instantaneous to continuous, and grain growth changes from one-dimensional to two-dimensional and then three-dimensional [49, 50]. The value of n_A around 2 shows that in this study, nucleation occurs on the grains and twin edges generally. Shaban and Eghbali [51] in a study on a micro-alloyed low-carbon steel containing Ti and Nb, and Liu et al. [52] in a study on low-carbon steel, reported Avrami exponent n_A equals to 2 and 1.8, respectively. Therefore, in both types of research, the recrystallization behavior of steels was estimated to be similar to our investigation, even though there are differences in the chemical composition and there is no boron as an alloying element in those two studies.

3.5. Microstructural Investigation

Figure 10-a shows the SEM image of the microstructure of the sample before deformation, which includes the main phase of ferrite, pearlite with a layered structure that is shown by the letter A and precipitates that are shown by the letter B, visible in the prior austenite grain boundaries (PAGB). Figure 10-b shows the results of EDS related to precipitates. According to this analysis, this phase is mainly composed of Fe, B and C elements with weight percent 62.5, 11.8 and 23.5, and atomic percent of 26.02, 25.33, and 45.49 respectively. According to the combination of alloying elements in the studied alloy and these precipitates, they can be a combination of cementite and boron carbide with the composition of $Fe_{23}(B, C)_6$, which is commonly formed in these alloys on the prior austenite grain boundaries [3, 5].

As mentioned earlier, since the percentage of light elements like B and C can't be measured accurately by EDS, the results of the thermodynamic analysis of JMatPro software in Figure 11 show that it is possible to form the boron carbide in the equilibrium state.
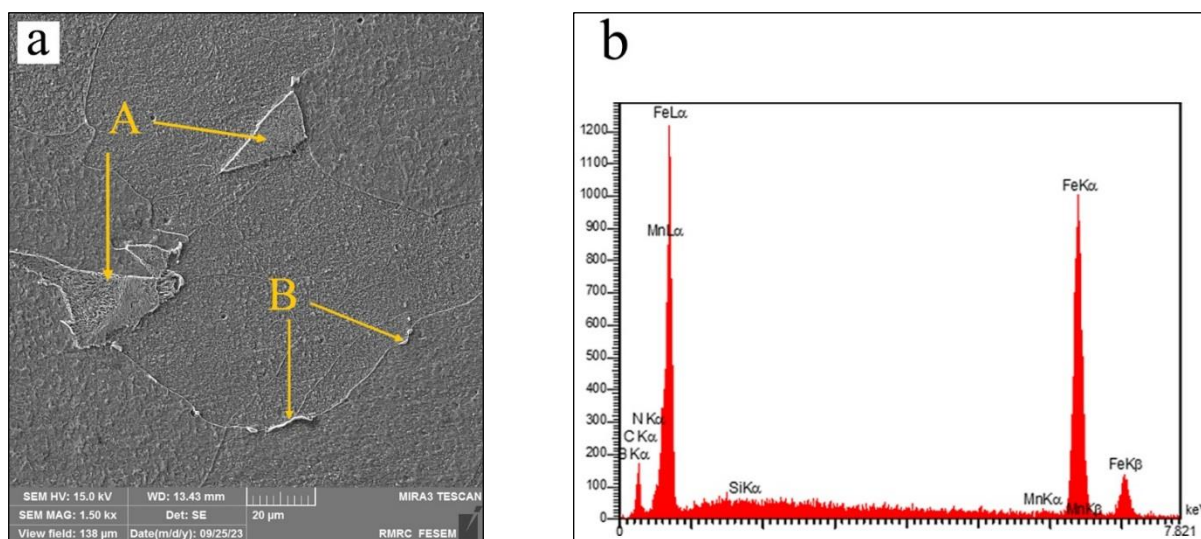

Fig. 10. a) SEM image of the microstructure of the sample, b) EDS analysis of the precipitates (B)

Fig. 11. Possible precipitates that can be formed in the equilibrium condition

In addition, the segregation of boron in grain boundaries has also been proven as non-equilibrium segregation [3], and therefore there is a possibility of boron segregation in grain boundaries and the formation of the mentioned precipitates. In addition, according to the results in Figure 11, other precipitates, including MnS, BN, TiN, TiB$_2$, AlN and Nb(C, N) were also possible to form in the equilibrium condition, but they may not have formed due to the non-equilibrium conditions in the production of the alloy, or due to the accuracy of the SEM, it is not possible to identify fine precipitates particles such as AlN and Nb(C, N).

Figure 12 shows the microstructures of the hot compression samples at temperatures of 950, 1050 and 1150°C at different strain rates, in which the loading direction is from top towards bottom. According to these pictures, at 950°C, the microstructure consists of recrystallized and elongated grains due to deformation, and the fraction of recrystallized equiaxed grains is lower than other samples, and with the increase of the strain rate, the number of DRX grains decreases. Compared to higher temperatures, at this temperature, the activity of softening mechanisms is less and its effect can be seen in the microstructure. In addition, it can be seen that the location of newly fine DRX grains is in the prior austenite grain boundaries (a number of them are shown with red arrows in Figure 12-a), which is in agreement with the results of the modelling of recrystallization behavior in the previous section. As the temperature increases

to 1050 and 1150°C, the fraction of equiaxed recrystallized grains increases significantly, and due to the favorable conditions, the growth of the grains also happens relatively and the newly recrystallized grains in the grain boundaries are less and can't be distinguished from the primary grains, and a larger part of the microstructure has recrystallized. By analyzing the microstructure images of the samples using MIP software, the average grain size for three compression test samples at 950, 1050 and 1150°C and strain rate 0.1 s^{-1} was measured as 21.9, 30.4 and 33.6 μm, and at strain rate 1 s^{-1} was measured as 17.7, 28.7 and 31.3 μm respectively. The grain size distribution was also obtained according to Figure 13. It can be seen that the grain size distribution has become more uniform with the increase of the deformation temperature, the average grain size has decreased and more grain refinement has occurred in the microstructure. Therefore, the microstructure of these samples is similar to DRX with a more uniform grain size distribution. Also, in general, it can be seen that with increasing temperature and decreasing strain rate, or in other words, decreasing the Zener-Hollmon parameter, the grain size becomes larger and grain boundaries become coarser, and vice versa.

4. CONCLUSIONS

The hot deformation and dynamic recrystallization behavior of boron-bearing low-carbon steel were modelled based on experimental data obtained from hot compression flow curves. The key findings are summarized as follows:

14

Fig. 12. OM images of the microstructure of hot compression samples, at (a, b) 950°C, (c, d) 1050°C, and (e, f) 1150°C, and strain rates 1 and 0.1 s⁻¹ respectively

1. Among the Arrhenius models used to calculate material constants and constitutive equations, the hyperbolic sine model provided a more accurate fit of the experimental data than the power model and the exponential model, which in the range of low and high strains, The R^2 values are closer to 1.

2. Deformation activation energy for the investigated steel in this study, the value of Q= 293.37 KJ/mol was obtained using the hyperbolic sine relationship, which is lower than the values obtained with the other two models, and a total difference of about 20 KJ/mol was calculated between the obtained activation energies. As a result, by obtaining the values and constants of the Arrhenius relations, the characteristic equation of the material was obtained.

3. After obtaining the hypothetical recovery curve for each sample and using other material parameters including the steady state stress, the recrystallization fraction was obtained for each sample. The recrystallization fraction data shows that with increasing temperature

and decreasing strain rate, the value of recrystallization fraction increases towards the value of 1 and recrystallization initiates at lower strains.

4. Numerical modelling of X_{DRX} data was done using the KJMA equation, which accurately shows the relationship between recrystallization fraction values and time, and the value of Avrami exponent for this steel was measured around 2. According to this value and referring to the recrystallization behavior prediction data tables, nucleation in the grain boundary regions is the usual mechanism of nucleation in this sample.

5. Based on the microstructural investigations using SEM, OM, and MIP software, the alloy's initial microstructure featured ferrite, pearlite with cementite, and boron carbide precipitates along prior austenite grain boundaries. Post hot compression tests at 950°C revealed recrystallized grains, with fewer equiaxed grains observed than at higher temperatures. At 1050 and 1150°C, the microstructures predominantly comprised recrystallized equiaxed grains with a more uniform distribution and finer average grain sizes of 30.4 µm and 33.6 µm respectively at a strain rate of 0.1 s^{-1}, with strain rate 1 s^{-1}, 28.7 and 31.3 µm were measured.

Fig. 13. Grain size distribution of hot compression samples, at (a, b) 950°C, (c, d) 1050°C, and (e, f) 1150°C, and strain rates 1 and 0.1 s^{-1} respectively

DATA AVAILABILITY

The data that support the findings of this study are available from the corresponding author, E. Mohammad Sharifi, upon reasonable request.

REFERENCES

[1]. Lu, Y., Effect of boron on microstructure and mechanical properties of low carbon microalloyed steels, McGill University, Montreal, Canada, 2007, 1-15.

[2]. Güler, H., Ertan, R., and Özcan, R., "Investigation of the hot ductility of a high-strength boron steel" Materials Science & Engineering A, 2014, 608, 90-94.

[3]. DaRosa, G., Maugis, P., Portavoce, A., Drillet, J., Valle, N., Lentzen, E., and Hoummada, K., "Grain-boundary segregation of boron in high-strength steel studied by nano-SIMS and atom probe tomography" Acta Materialia, 2020, 182, 226-234.

[4]. Suski, C. A., and Oliveira, C. A. S., "Effect of austenitization temperature on the precipitation of carbides in quenched low carbon boron steel" Metallorgy and Microstructral Analysis, 2013, 79-87.

[5]. Li, Y. J., Ponge, D., Choi, P., and Raabe, D., "Segregation of boron at prior austenite grain boundaries in a quenched martensitic steel studied by atom probe tomography" Scripta Materialia,2015, 96, 13-16.

[6]. Liu, W., Li, J., Shi, C., and Yu, L., "Influence of boron addition on the hot ductility of low-carbon aluminum-killed steel" Materials Transactions, 2015, 56, 1133-1139.

[7]. Perez, R., Garcia, A., and Juarez, J. A., "On the structural characteristics of precipitates in boron microalloyed steels" Scripta Metallurgica et Materialia, 1993, 28, 931-936.

[8]. Deva, A., Jha, N. K., and Jha, B. K., "Effect of austenitising temperature and cooling condition on mechanical properties of low carbon boron containing steel" International Journal of Metallurgical Engineering, 2012, 1, 1-6.

[9]. Koley, S., Karani, A., Chatterjee, S., and Shome, M., "Influence of boron on austenite to ferrite transformation behavior of low carbon steel under continuous cooling" Journal of Materials Engineering and Performance, 2018, 11, 300-308.

[10]. Suzuki, S., Tanino, M., and Waseda, Y., "Phosphorus and boron segregation at prior austenite grain boundaries in low-alloyed steel" ISIJ International, 2002, 42, 676-678.

[11]. Terzic, A., Calcagnotto, M., Guk, S., Schulz, T., and Kawalla, R., "Influence of Boron on transformation behavior during continuous cooling of low alloyed steels" Materials Science & Engineering A, 2013, 584, 32-40.

[12]. Deva, A., Jha, B. K., and Mishra, N. S., "Microstructural evolution during batch annealing of boron containing aluminum-killed steel" Journal of Material Science, 2009, 44, 3736-3740.

[13]. Ma, X., Miao, C., Langelier, B., and Subramanian, S., "Suppression of strain-induced precipitation of NbC by epitaxial growth of NbC on pre-existing TiN in Nb-Ti microalloyed steel" Materials & Design, 2017, 132, 244-249.

[14]. Ghosh, S., Singh, A. K., Mula, S., Chanda, P., Mahashabde, V. V., and Roy, T. K., "Mechanical properties, formability and corrosion resistance of thermomechanically controlled processed Ti-Nb stabilized IF steel" Materials Science & Engineering A, 2017, 684, 22-36.

[15]. Ali, M., Nyo, T., Kaijalainen, A., Javaheri, V., Tervo, H., Hannula, J., Somani, M., and Kömi, J., "Incompatible effects of B and B+Nb additions and inclusions' characteristics on the microstructures and mechanical properties of low-carbon steels" Materials Science & Engineering A, 2021, 819, 141-153.

[16]. Murari, F. D., da Costa, A. L. V., Silva, E., and de Avillez, R. R., "Cold-rolled multiphase boron steels: microstructure and mechanical properties" Journal of Material Research and Technology, 2015, 4, 191-196.

[17]. Huang, K., and Logé, R.E., "A review of dynamic recrystallization phenomena in metallic materials" Materials & Design, 2016, 111, 548-574.

[18]. Lin, Y. C., Chen, M. S., and Zhong, J., "Prediction of 42CrMo steel flow stress

17

at high temperature and strain rate" Mechanics Research Communications, 2008, 35, 142-150.

[19]. Lin, Y.C., and Chen, X. M., "A critical review of experimental results and constitutive descriptions for metals and alloys in hot working" Materials & Design, 2011, 32, 1733-1759.

[20]. Mirzadeh, H., "Grain refinement of magnesium alloys by dynamic recrystallization (DRX): A review" Journal of Materials Research and Technology, 2023, 25, 7050-7077.

[21]. Mirzadeh, H., "Quantification of the strengthening effect of reinforcements during hot deformation of aluminum-based composites" Materials & Design, 2015, 65, 80-82.

[22]. Sakai, T., Belyakov, A., Kaibyshev, R., Miura, H., and Jonas, J. J., "Dynamic and post-dynamic recrystallization under hot, cold and severe plastic deformation conditions" Progress in Materials Science, 2014, 60, 130-207.

[23]. Lin, Y. C., Chen, M. S., and Zhang, J., "Modeling of flow stress of 42CrMo steel under hot compression" Materials Science and Engineering: A, 2009, 499, 88-92.

[24]. Yada, H., "Prediction of microstructural changes and mechanical properties in hot strip rolling" Proceedings of the Metallurgical Society of the Canadian Institute of Mining and Metallurgy, 1988, 1, 105-119.

[25]. Laasraoui, A., and Jonas, J. J., "Recrystallization of austenite after deformation at high temperatures and strain rates-analysis and modeling" Metallurgical, 1991, 22, 151-160.

[26]. Kim, S. I., and Yoo, Y. C., "Dynamic recrystallization behavior of AISI 304 stainless steel" Materials Science and Engineering: A, 2001, 311, 108-113.

[27]. Kim, S. I., Lee, Y., Lee, D. L., and Yoo, Y. C., "Modeling of AGS and recrystallized fraction of microalloyed medium carbon steel during hot deformation" Materials Science and Engineering: A, 2003, 355, 384-393.

[28]. Shen, W., Zhang, C., Zhang, L., Xu, Q., and Cui, Y., "Experimental Study on the Hot Deformation Characterization of Low-Carbon Nb-V-Ti Microalloyed Steel" Journal of Materials Engineering and Performance, 2018, 27, 4616-4624.

[29]. Shkatov, V., and Mazur, I., "Modeling the Dynamic Recrystallization and Flow Curves Using the Kinetics of Static Recrystallization" Materials, 2019, 12, 1-15.

[30]. Zhao, H., Qi, J., Liu, G., Su, R., and Sun, Z., "A comparative study on hot deformation behaviors of low-carbon and medium-carbon vanadium microalloyed steels" Journal of Materials Research and Technology, 2020, 9, 5, 11319-11331.

[31]. Stumpf, W., and Banks, K., "The hot working characteristics of a boron bearing and a conventional low carbon steel" Materials Science and Engineering A, 2006, 418, 86-94.

[32]. Mielnik, E., Metalworking science and engineering, New York, USA, 1991, 1-50.

[33]. Evans, R. W., and Scharning, P. J., "Axisymmetric compression test and hot working properties of alloys" Materials Science and Technology, 2001, 17, 995-1004.

[34]. Ebrahimi, R., and Najafizadeh, A., "A new method for evaluation of friction in bulk metal forming" Journal of Materials Processing Technology, 2004, 152, 136-143.

[35]. Zhao, D., ASM handbook: Mechanical testing and evaluation, ASM International, Ohio, USA, 2000, 798-810.

[36]. Goetz, R. L., and Semiatin, S. L., "The adiabatic correction factor for deformation heating during the uniaxial compression test" Journal of Materials Engineering and Performance, 2001, 10, 710-717.

[37]. Shahriari, B., Vafaei, R., Sharifi, E. M., and Farmanesh, Kh, "Modeling Deformation Flow Curves and Dynamic Recrystallization of BA 160 Steel During Hot Compression" Metals and Materials International, 2018, 24, 955-969.

[38]. Fernández, A. I., Uranga, P., López, B., and Rodriguez-Ibabe, J. M., "Dynamic recrystallization behavior covering a wide austenite grain size range in Nb and Nb–Ti microalloyed steels" Materials Science and Engineering: A, 2003, 361, 367-376.

[39]. Yan, N., Li, Z., Xu, Y., and Meyers, M. A.,

"Shear localization in metallic materials at high strain rates" Progress in Materials Science, 2021, 119, 1879-1912.

[40]. Cottrell, A.H., and Bilby, B., "Dislocation theory of yielding and strain ageing of iron" Proceedings of the Physical Society A, 1949, 1, 49-62.

[41]. Deva, A., Jha, B. K., and Mishra, N. S., "Influence of boron on strain hardening behavior and ductility of low carbon hot rolled steel" Materials Science and Engineering A, 2011, 528, 7375-7380.

[42]. Choudhary, B. K., and Christopher, J., "Influence of temperature and strain rate on tensile deformation and fracture behavior of boron added P91 steel" International Journal of Pressure Vessels and Piping, 2019, 171, 153-161.

[43]. Humphreys, F. J., and Hatherly, M., Recrystallization and related annealing phenomena, Elsevier Science, Amsterdam, Netherland, 2004, 121-167.

[44]. Cho, K. C., Mun, D. J., Kim, J. Y., Park, J. K., Lee, J. S., and Koo, Y. M., "Effect of boron precipitation behavior on the hot ductility of boron containing steel" Metallurgical and material transactions A, 2010, 41, 1421-1428.

[45]. Poliak, E.I., and Jonas, J. J., "A one-parameter approach to determining the critical conditions for the initiation of dynamic recrystallization" Acta Materialia, 1996, 44, 127-136.

[46]. Estrin, Y., and Mecking, H., "A unified phenomenological description of work hardening and creep based on one-parameter models" Acta Metallurgica0 1984, 32, 57-70.

[47]. Jonas, J. J., Quelennec, X., Jiang, L., and Martin, É., "The avrami kinetics of dynamic recrystallization" Acta Materialia, 2009, 57, 2748-2756.

[48]. Rollett, A. Rohrer, G. S., and Humphreys, J., Recrystallization and related annealing phenomena, Elsevier, New York, USA, 2017, 54-101.

[49]. Christian, J. W., The Theory of Transformations in Metals and Alloys, University of Oxford, Oxford, UK, 2002, 21-60.

[50]. Rezaei, J., Parsa, M. H., and Mirzadeh, H., "Phase transformation kinetics of high-carbon steel during continuous heating" Journal of Materials Research and Technology, 2023, 27, 2524-2537.

[51]. Shaban, M., and Eghbali, B., "Determination of critical conditions for dynamic recrystallization of a microalloyed steel" Materials Science and Engineering A, 2010, 527, 4320-4325.

[52]. Liu, C., Peng, Y., Barella, S., Mapelli, C., and Liang, S., "Characterization of dynamic recrystallization behavior of low carbon steel under flexible rolling process" Materials Today Communications, 2021, 29, 1-21.